Peer-reviewed version available at Materials 2019, 12, 1885; doi:10.3390/ma12121885

Article

A multiscale modelling approach for estimating the effect of defects in unidirectional carbon fiber reinforced polymer composites

Kim-Niklas Antin [1], Anssi Laukkanen [2], Tom Andersson [2], Danny Smyl [3] and Pedro Vilaça [1,*]

[1] Aalto University, Department of Mechanical Engineering, Puumiehenkuja 3, 02150 ESPOO, Finland; kim-niklas.antin@aalto.fi
[2] VTT Technical Research Centre of Finland, Kivimiehentie 3, 02044 VTT, Finland; anssi.laukkanen@vtt.fi
[3] University of Sheffield, Department of Civil and Structural Engineering, Mappin Street, S13JD Sheffield, United Kingdom; d.smyl@sheffield.ac.uk
* Correspondence: pedro.vilaca@aalto.fi

Abstract: A multiscale modelling approach was developed in order to estimate the effect of defects on the strength of unidirectional carbon fiber composites. The work encompasses a micromechanics approach, where the known reinforcement and matrix properties are experimentally verified and a 3D finite element model is meshed directly from micrographs. Boundary conditions for loading the micromechanical model are derived from macroscale finite element simulations of the component in question. Using a microscale model based on the actual microstructure, material parameters and load case allows realistic estimation of the effect of a defect. The modelling approach was tested with a unidirectional carbon fiber composite beam, from which the micromechanical model was created and experimentally validated. The effect of porosity was simulated using a resin-rich area in the microstructure and the results were compared to experimental work on samples containing pores.

Keywords: Modelling; Carbon fiber composite; Experimental mechanics; Multiscale; Defect

1. Introduction

Fiber reinforced polymers are important materials for structural applications in many fields. For example, there are several notable applications of unidirectional (UD) carbon fiber reinforced polymers (CFRP) in civil engineering [1-4]. Various mathematical regimes, including analytical [5-6], semi-analytical [7], and numerical models [8], have been formulated to estimate the strength of these materials [9]. Homogenised macroscale models [10] do not correctly capture the failure mechanisms of a composite material and therefore micromechanical models have been developed as an alternative [11]. Micromechanical models can be divided into phenomenological models, such as shear lag and fiber bundle models [12], and numerical models using the finite element method [9]. Although both types of micromechanical models take into account the interactions between fiber and matrix, only numerical models have the potential to fully capture the complex nature of damage evolution in composites [13]. They have the capability of accurately describing how failure starts and how defects, that are small compared to the microstructural features, affect the performance of a composite. Numerical micromodels can also be used to solve ply properties without experimental work when designing laminates. Several analytical models have been developed for solving the homogenised properties based on constituent properties [14]. However, the analytical models do not always perform reliably, especially when fiber volume fractions are higher than 0.6 [15]. The analytical solutions are, however, simple to use. These homogenised macroscopic material properties are needed as an input for computation of mechanical finite element models. Micromechanical modelling

Peer-reviewed version available at Materials 2019, 12, 1885; doi:10.3390/ma12121885

is useful during the service life of a component as well. It could provide a means to simulate the response of a structure as a function of different sizes and types of damage occurring during service, and hence be integrated in relevant condition monitoring systems. It also allows for continued assessment and provides better information as to the required actions when damage is found and characterized via non-destructive evaluation [16]. In other words, it furthers the ability to determine the residual strength and evaluate whether or not a component can continue in service. However, micromechanical models require the correct input, namely fiber and matrix properties (constituent properties) and microstructure, in order to deliver reliable results.

Obtaining constituent properties and validating the homogenised output is not straightforward for anisotropic composite materials. However, transversely isotropic materials like carbon fiber and unidirectional fiber-reinforced composites have only five independent material constants [17]. The longitudinal Young's modulus E_{1f} of the fiber is straightforward to calculate from instrumented tensile tests [18-19]. Furthermore, the rule of mixtures is well established for axial properties of UD composites and allows inverse micromechanics to be used with confidence. Direct measurements of transverse Young's modulus E_{2f} have been conducted using nanoindentation [14] and the results were found to be slightly higher than those obtained using various analytical inverse micromechanics solutions [20]. Resonance frequencies have also been used to measure transverse Young's modulus of carbon fibers [21]. Obtaining experimentally the remaining three elastic constants of a single filament is challenging. Many authors resort to measuring composite properties and using inverse micromechanics [22]. Some modelling papers simply assume certain elastic properties [22-24] while others cite sources which are difficult to obtain [25].

The modelled microstructure should describe information such as fiber volume fraction, packing, size and shape as accurately as possible. Periodic square or hexagonal fiber packing is an idealized case whereas random packing generators create a more realistic distribution of fibers [26], but high fiber volume fractions are challenging for the generators [27]. There is an effect on transverse elastic constants between periodic and random packing [15]. In strength models, fibers very close to each other can lead to a significant increase in stress concentration factors [26], but the stress recovery distance is smaller due to a locally stiffer matrix. Hence, packing type does not make much of a difference for uniaxial loading of UD CFRPs in the fiber direction [28]. However, matrix plasticity and debonding may change results [29] and off-axis loading requires random packing for accurate results [30].

This paper describes the creation of a multiscale microstructure-based model and the experimental validation of it. Ultimately, the goal of this work is to create a macroscale strength model that considers microstructural defects without the need for experimental model updating or calibration. The structure of the paper is as follows. First, the general structure of the multiscale approach and the pre-requisites for a micromechanical model are described. Second, the numerical methods for calculating composite properties using the information established in the previous step are presented. Third, the composite properties are used to obtain relevant boundary conditions for loading the original micromodel and simulating the effect of a defect on strength. The modelling results are compared to measurements of a pultruded UD CFPR beam at each step.

2. Materials and Methods

The workflow (Figure 1) follows a typical multiscale approach [31] where microscopic behaviour is described using a representative volume element (RVE) and global response is simulated using homogenisation of the RVE (first step). Statistical representation of the microstructure is evaluated by varying the RVE size until stabilization of homogenised properties occurs. The sensitivity of the homogenised properties to changes in constituent properties, i.e. fiber and matrix properties, are analysed with the aim of assessing the importance of individual input parameters, since not all of them are necessarily well known. Homogenised properties can be measured experimentally [32], but the goal here is that no experimental calibration [33] or inverse micromechanics is used. There are two reasons for this. First, experimental work can be expensive and time-consuming if it is needed every time an input parameter changes. Second, using inverse micromechanics or model calibration

Peer-reviewed version available at Materials 2019, 12, 1885; doi:10.3390/ma12121885

makes experimental validation redundant. The second step in the workflow is to insert the homogenised properties into a macroscopic model, which takes the component geometry, boundary conditions and load cases into consideration. The response of the macroscopic model can be validated experimentally by loading the component and comparing measured strain values with simulated strain. The macroscopic model is used to identify critical areas in the structure. The third step in the workflow involves using the critical locations for defining displacements and boundary conditions for the RVE so that they are relevant with the practical application in mind. The effect of known defects found using advanced NDE [16] or postulated defects can now be evaluated in microscale with loading conditions relevant to real-life applications. The simulated failure strength of a defective component can thus be calculated and compared to experimentally obtained failure loads. Ideally, this process allows the estimation of residual strength of a defective component based on in-service inspection results.

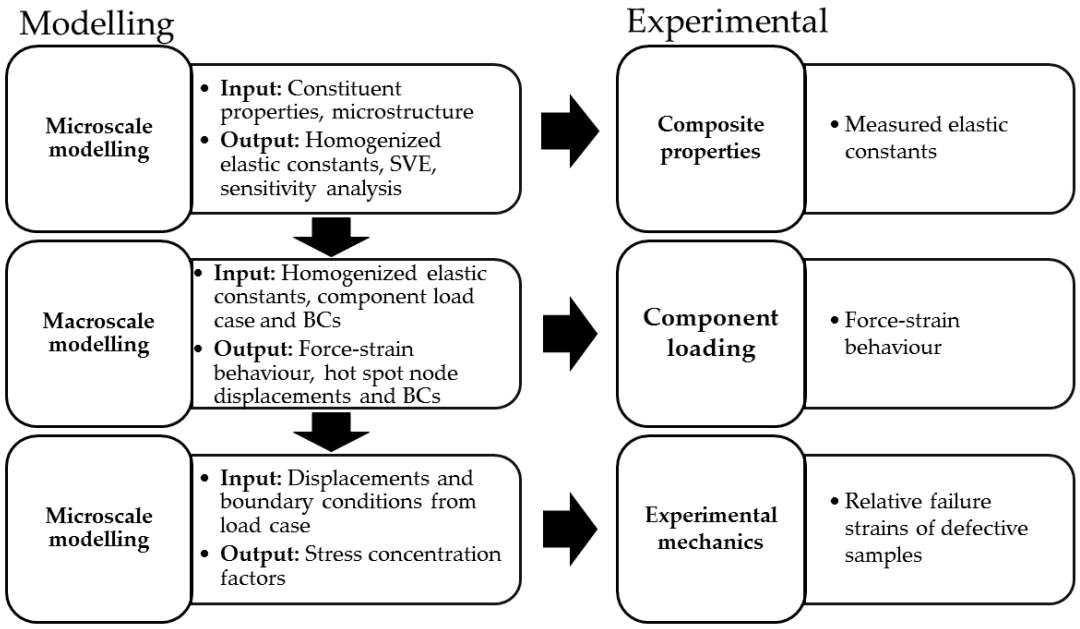

Figure 1. Flow chart describing the modelling process with concurrent experimental work.

The macroscopic model and case study presented in this paper is three point bending of a pultruded UD CFRP beam. Constituent properties and micrographs are used to create the RVE and to obtain homogenised composite properties. The critical location is identified from the macroscopic simulation results and the node displacements at that location are used as a load case for the RVE to evaluate the effect of porosity on the strength of the beam. Experimental validation is done for each step.

2.1 Constituent properties

Constituent properties given by the manufacturer are used in this study, which is a typical source in modelling papers [34-35]. This paper uses E_1, E_2, G_{12}, ν_{12} and ν_{23}, because these are the most feasible to obtain experimentally. Here, fiber direction is denoted as "1" and the transverse plane as "2-3" (Figure 2).

Experimental verification of the given constituent properties were conducted where possible using instrumented nanoindentation. Indentation was performed using a CSM machine on longitudinal and transverse cross-sections of the UD CFRP material [40] with the intention of verifying E_{1f}, E_{2f} and E_m, where the subscripts "f" and "m" stand for fiber and matrix respectively. Specimen cross-sections were wet sanded to FEPA P4000 grit and ten measurements were made in a line with 10 μm intervals. An indentation depth of 0.1 μm was selected because the indentation

modulus stabilizes at relatively high values [14,36-37]. On the other hand, deeper indentation was avoided in order to keep the area function of the sphero-conical tip continuous and to avoid fracture. It was apparent from the results which indentations had hit the fiber and which were on the matrix (Figure 4). For the transverse sample, the direction of the measurement line was perpendicular to fiber direction meaning that no two measurements are from the same filament. The indentation parameter are: Indenter = SB-B28 sphero-conical; Tip radius = 2 μm; Cone full angle = 90°; Indentation depth = 0.1 μm; (un)Loading rate = 0.8mN/min; Dwell time = 30 s; Data acquisition rate = 10 Hz.

The initial unloading slope was determined from the force-displacement data. The typically used power-law fit proposed by Oliver & Pharr [38] did not produce high-correlation fits and therefore a quadratic polynomial was used. Any permanent displacement (h_f) was subtracted from the data and intersection with the origin was imposed. The derivative of the polynomial fit at maximum displacement was used to obtain the initial unloading slope or contact stiffness, S [39]. The contact stiffness was used to calculate the contact depth (h_c) using parameter ε=0.75 as proposed in [38]. The contact depth was used to calculate the projected contact area and thus the indentation modulus M as defined by Vlassak [40]. The indentation modulus of the isotropic matrix is straightforward to calculate using the Oliver & Pharr method [38] when the indenter properties are known. For an anisotropic material, where the contact area is elliptical, another solution is used [41-42]. The principle there is to solve all five stiffness constants using a five-equation system by inserting three previously known stiffness constants and two perpendicular indentation results. A one-at-a-time sensitivity analysis showed that none of the inserted engineering constants alone affects the results to a significant extent. The sensitivity analysis was conducted by doubling or halving each engineering constant one at a time. The resulting values for E_{2f} were maintained within 10% of the reference case. The indentation modulus had the largest effect, which was close to a linear dependency.

2.2 Microstructure

Since the ultimate goal here is a strength model, real microstructure of a pultruded CFRP beam is used to generate the model morphology. High-resolution X-ray microtomography has been conducted on the pultruded CFRP material [16]. However, distinguishing between fiber and matrix from microtomography voxel data was found to be unreliable and therefore a 2.5D approach was selected. Completely straight fibers are assumed although the tomography data [16] and transverse cross-sections [3] indicate some fiber waviness. 2D data from cross-sections imaged using variable pressure scanning electron microscopy (VP-SEM) and backscatter electron (BSE) detection are used. The incident electrons were accelerated with a potential of 25 kV in order to get a higher yield of back-scattered electrons compared to lower acceleration voltages. Fiber volume fraction is analysed from that image as well using a binary colour map and manually adjusted threshold criteria. Defects were introduced to the pultruded material by adding water to the resin bath at the pultrusion line. Optical microscopy was used to characterize the resulting pore content and typical pore size, but the 2.5D approach for generating a 3D mesh does not allow using direct image-based meshing for the microstructure containing pores. Instead, a resin-rich area of the microstructure is used to represent the effect of porosity.

2.3 Microscale modelling

An image-based approach is used to obtain a representative microstructure for further micromechanical analysis. SEM images were segmented initially to a two-phase depiction of the material, the fiber and resin phases, respectively. In order to improve the realism of modelling and eliminate possible artefacts from SEM specimen preparation, individual fibers were detached algorithmically. These two-dimensional segmented images were extruded to yield a cubic representative volume element (RVE) of the composite. As image-based meshing was utilized, no geometric representative of the microstructure was generated at any point, but rather, the segmented data is meshed directly. In addition to the fiber and resin phases, an interface region is included (interphase) (Figure 2). The strategy chosen in the current work is to include the interface firstly to

obtain separation of individual fibers and secondly to yield a better description of the composite microstructure and interaction between the fibers and the resin [43-44]. The approach falls within effective interface approaches, i.e. the interface is a third phase, which effectively captures the interface region behaviour between fibers and resin by employing its own mechanical material properties. Further details of the modelling toolset utilized in creating the interphase are presented in [31].

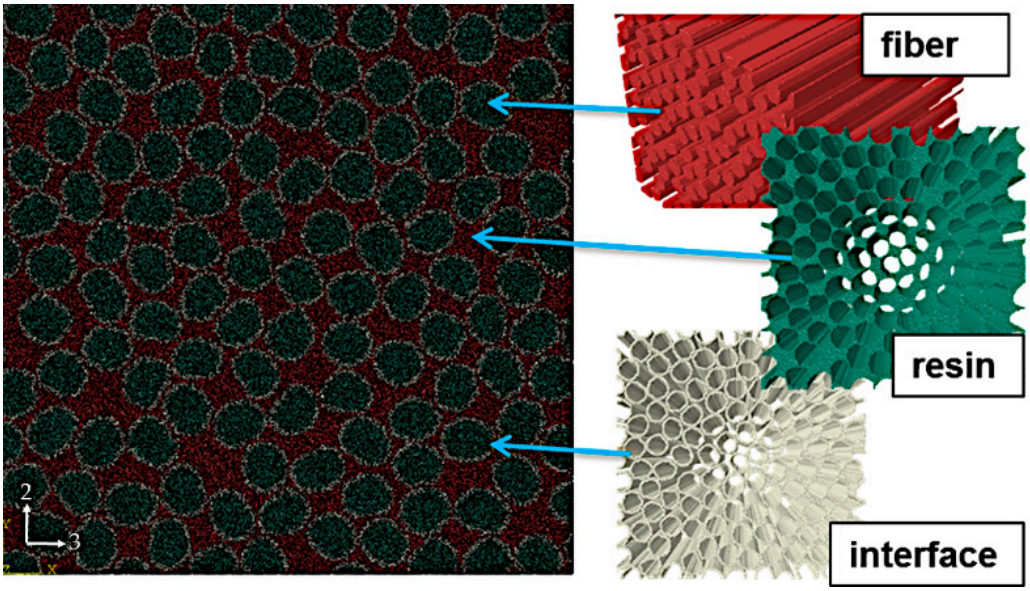

Figure 2. Representation of the three-phase microstructure: algorithmically detached fibers, interface (interphase) added to the fiber perimeters and resin filling the rest.

Numerical homogenisation was employed in determining the engineering material properties of the composite based on micromechanical modelling results. The RVEs were loaded under kinetic-uniform boundary conditions (KUBC) and subjected to differing imposed strain states to compute the volume averaged metrics for solving the composite material properties. In addition, the computational volume from which the data was extracted was considered a variable in order to ascertain that the RVE size is representative of composite behaviour. This was carried out by sampling increasing material volumes beginning from the center of the microstructure towards its external boundaries and assessing the changes in material property predictions.

The homogenised composite properties obtained with microscale FE modelling were compared to analytical micromechanical equations. Results using the equations by Chamis [39] are included as a comparison, since those equations require only the fiber volume fraction in addition to the constituent properties. Other models often require some empirical parameters for the material in question [17], which is effectively model calibration.

All of the homogenised composite properties were verified experimentally. The parameters E_1 and ν_{12} were measured using uniaxial tensile and compression tests following the procedures in ISO 527-5, with strain gauges bonded parallel and perpendicular to fiber direction. The parameter ν_{12} was solved by linear regression of the ε_t-ε_L strain data instead of measuring transverse thickness of the sample as is suggested in the standard. E_2 and ν_{23} were obtained using micro-DIC (Digital Image Correlation) in transverse compression where the fibers themselves were used as contrast pattern. Furthermore, quasi-static elasticity imaging was used to solve E_1, E_2, ν_{12} and G_{12}. All of the previous macroscale experiments are explained in more detail in [45].

2.4 Macroscale modelling

The finite element method was used for simulating the macroscale behaviour of the UD CFRP beam. The simulations allow experimental verification of the behaviour of a real component using the

material constants obtained in the previous step. In addition, they give boundary conditions and node displacements for the micromodel that are relevant to a real loading situation. The three point bending setup used for experimental work was modelled and meshed in Abaqus CAE using quadratic tetrahedral (C3D10) elements (Figure 3). The rollers were defined as rigid shell bodies with Hertzian contact and a 0.15 friction coefficient [46]. Orthotropic material properties from the homogenised micromechanical model were used for material properties of the specimen. A load of 658 N was applied to the central roller, which corresponds to the forces seen in earlier experimental work [45]. In addition, cases with isotropic assumptions and a sensitivity analysis to individual material parameters was made. The results were compared to flexural tests according to ISO 14125, which are described in more detail in [45] and apparent interlaminar shear strength (ILSS) tests according to ISO 14130.

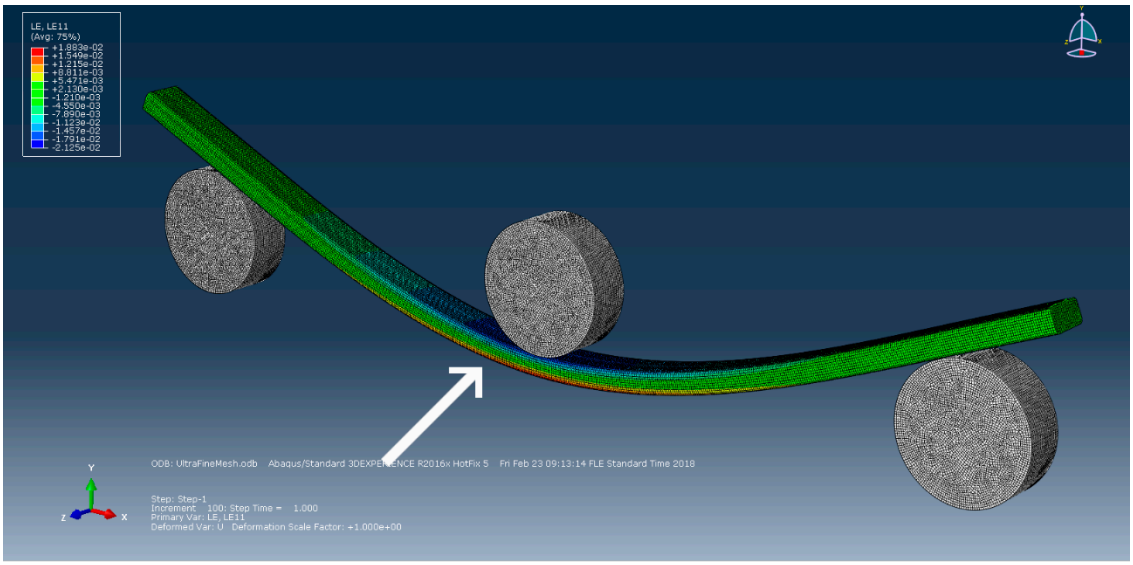

Figure 3. Location of strain hot spot in simulated three point bending.

3. Results

The results are presented following the simulation workflow. First, constituent properties given by the manufacturer are compared to measured values. The micrographs used for meshing are presented also. Second, the representative microstructure is created and homogenised to obtain composite properties. The results are compared to those obtained by analytical and experimental methods. Third, macroscale simulations are used to create relevant loads for the micromechanical model. Last, CFRP components are tested to failure and compared to the simulated stresses and strains of corresponding microstructures.

3.1. Constituent properties

The micromodel inputs are the constituent properties and microstructure. The manufacturer has provided material values for the constituents (Table 1). Only one shear modulus is used in this paper and therefore ν_{23f} needs to be calculated using the given value of G_{23f} considering the isotropic condition in the 2-3 plane.

Table 1. Material constants given by the manufacturer.

	E_1 [GPa]	E_2 [GPa]	G_{12} [GPa]	G_{23} [GPa]	ν_{12}	ν_{23} (calculated)
Fiber, f	239	20	30	8	0.2	0.25
Matrix, m	3.2				0.35	

Peer-reviewed version available at Materials 2019, 12, 1885; doi:10.3390/ma12121885

Nanoindentation was conducted in order to verify some of the given parameters (Figure 4). There is a large discrepancy between the Young's moduli obtained from indentation data and values reported by the composite manufacturer (Table 2). The reason for differing behavior in the case of the fiber is proposed to be nanobuckling and compressive failure in the nanostructure of carbon fiber [47]. Others have obtained similar results for PAN-based carbon fibers [37,48-50]. The resulting E_{2f} from these indentations is 13 GPa, which falls between the 20 GPa given by the manufacturer and inverse micromechanics [14,17] from transverse compression tests indicating E_{2f} should be 10 GPa. The reason for differing epoxy stiffness is attributed to the constraint imposed by surrounding fibers [50].

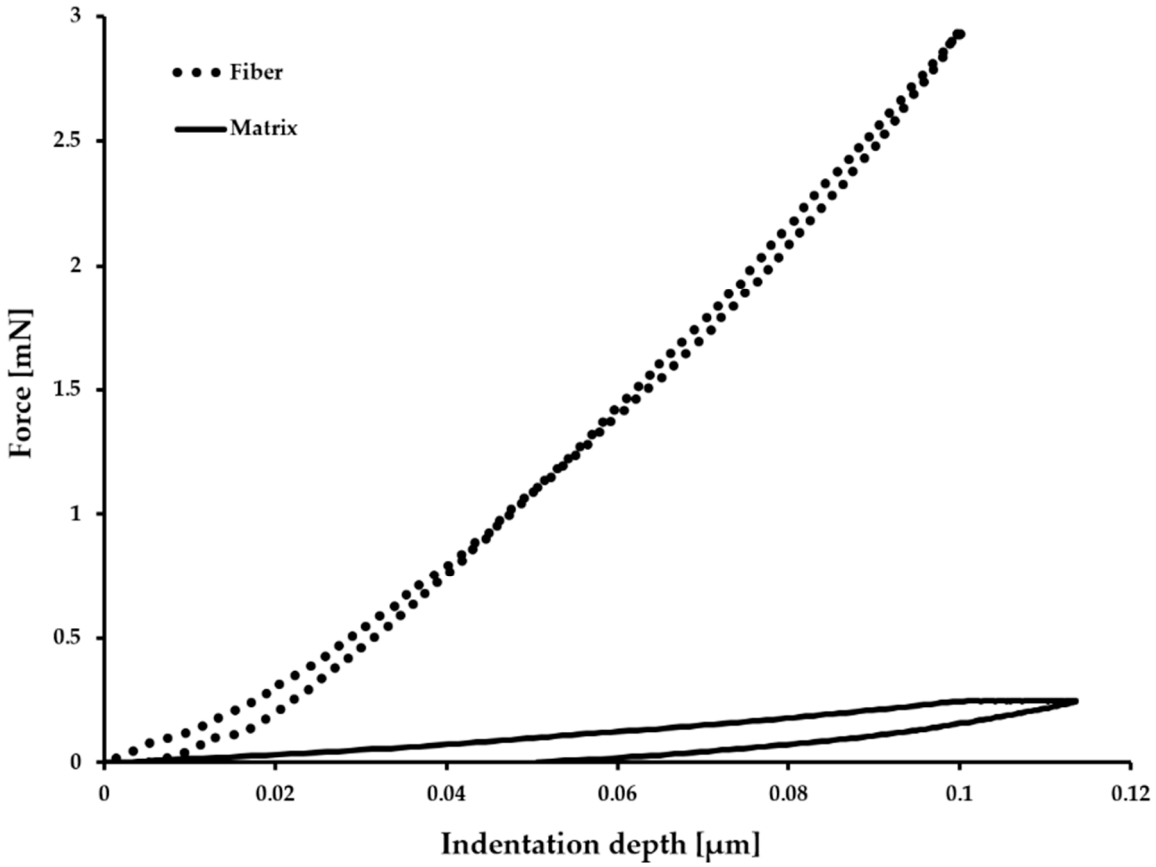

Figure 4. Loading/unloading curves of fiber and matrix from which indentation modulus is calculated.

Table 2. Comparison of indentation results with the given reference values.

	Contact stiffness, S [mN/μm]	Indentation modulus, M [GPa]	Young's modulus, E [GPa]	Reference, E [GPa]
Fiber, long.	46 ± 4	50	55	239
Fiber, trans.	17.5 ± 0.9	19	13	20
Matrix	13 ± 3	11	13	3

3.2 Microstructure

The microstructure obtained using electron microscopy (Figure 5) was processed algorithmically into a multiphase mesh. The fiber volume fraction was obtained from the segmenting process also. The fiber fraction was found to be 0.65, which corresponds to the fill ratio disclosed by the manufacturer. The introduced pores were characterized using light optical microscopy (Figure 6). The image shows clusters of multiple pores approximately 20 μm in diameter.

Peer-reviewed version available at *Materials* **2019**, *12*, 1885; doi:10.3390/ma12121885

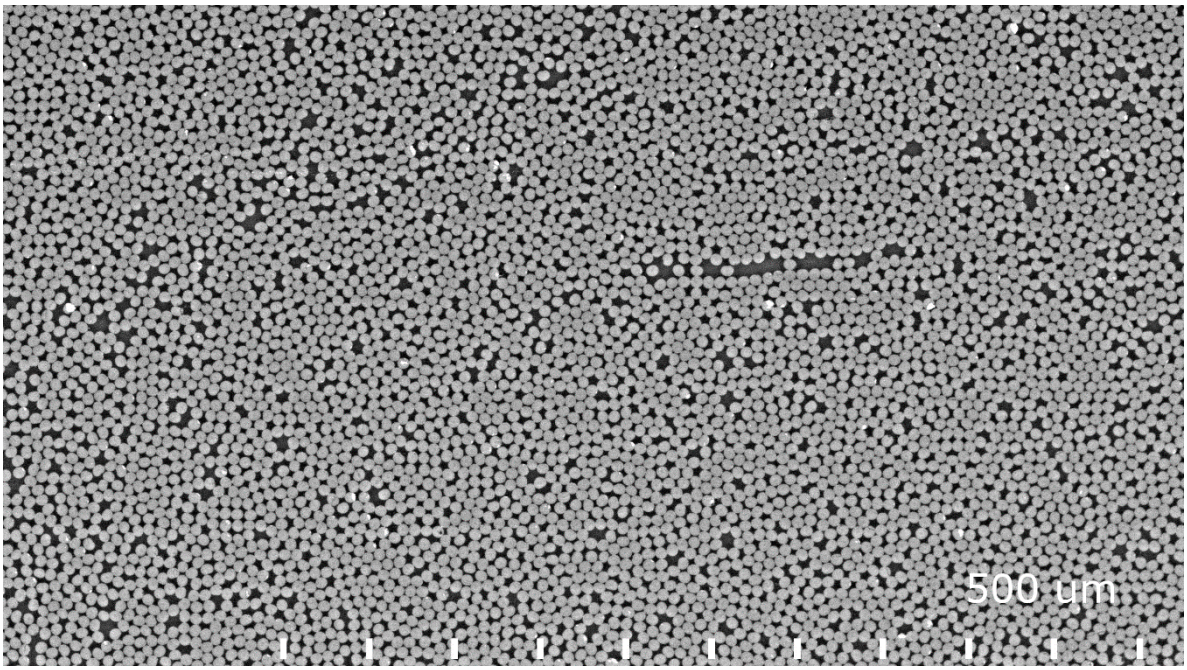

Figure 5. Electron backscatter image distinguishes between fiber and matrix due to a difference in average atomic number (Z contrast).

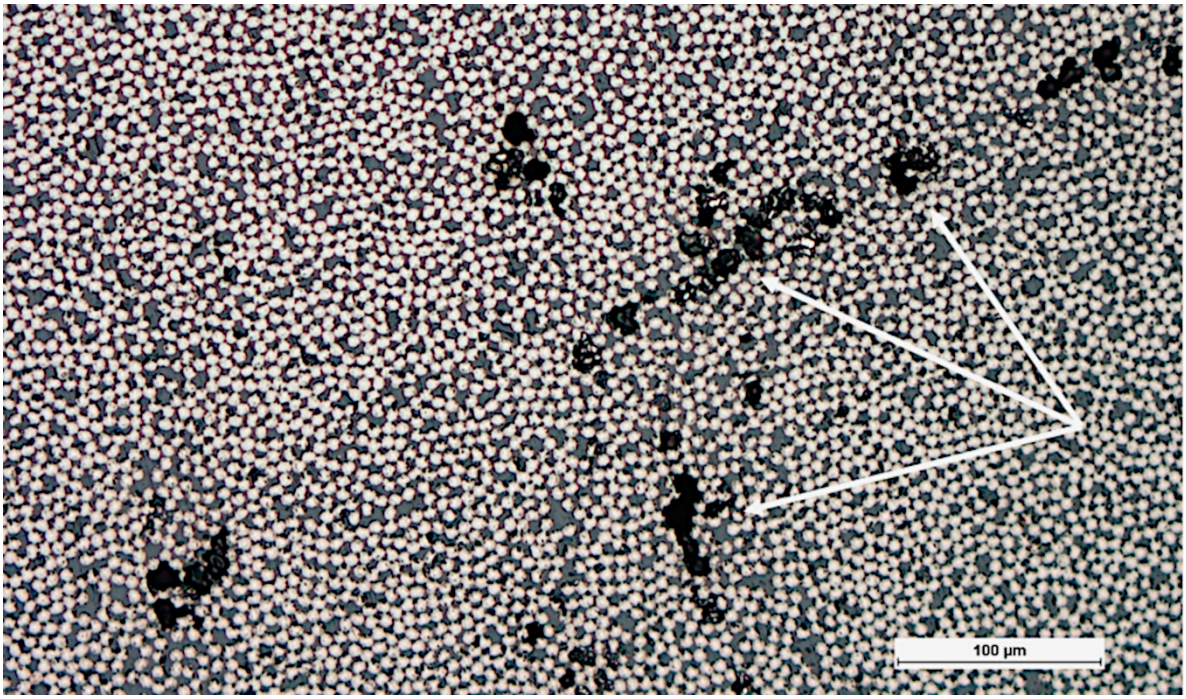

Figure 6. Optical micrograph showing pores (marked with white arrow).

3.3 Microscale modelling

The statistical representation of the microstructure meshed from the previous step (Figure 7) can be evaluated by looking at homogenised values as a function of volume fraction of total microstructure size. It is noted that stabilization of the prediction takes place at 0.5 of total volume, indicating that the system is representative with respect to property computation. In addition, it is noted that chosen boundary conditions for the simplistic description of material behavior do not markedly influence

Peer-reviewed version available at *Materials* **2019**, *12*, 1885; doi:10.3390/ma12121885

the computation, as no significant deviations in the predictions are visible as the volume fraction approaches 1.0.

A one-at-a-time sensitivity analysis was conducted using the micromechanical FE model. In total, 14 simulations were made and the resulting homogenised composite properties were analyzed in terms of the five independent composite constants. The relative change to the reference value was calculated and all ratios between 0.9-1.1 were omitted as insignificant. Ratios below 0.7 are marked with red indicating a significant reduction while values above 1.3 are marked with green indicating a significant increase. Values in between are marked with yellow to indicate a small change (Table 3). The most important constituent properties are E_{1f}, E_{2f}, G_{12f} and E_m while the Poisson's ratios do not have a strong effect on composite properties, especially when considering the realistic bounds for those values. E_1 is affected by E_{1f} while E_2 is affected by E_{2f} and E_m as shown also in the analytical formulation [20]. E_{1f} has a surprising effect on G_{12}, which is not included in the analytical model, which, on the other hand, exaggerates the role of E_m on G_{12}. The Poisson's ratio ν_{12} is insensitive to all parameters while ν_{23} changes with many of the parameters.

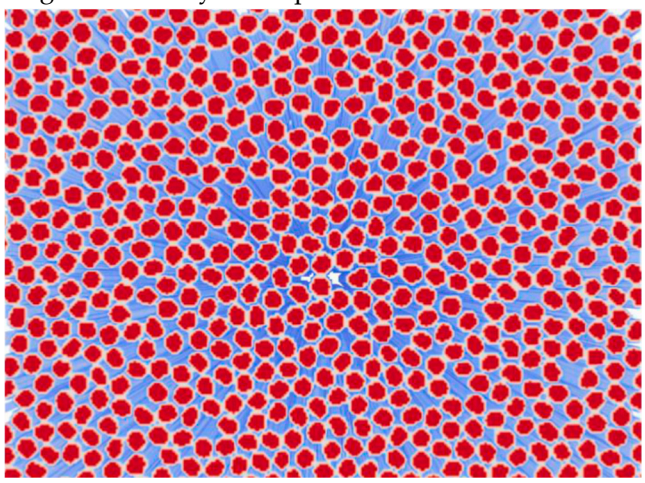

Figure 7. Image-based meshing of the microstructure showing a perspective view of the fiber and interphase.

Table 3. Sensitivity of homogenised composite properties to fiber and resin properties.

	Multiplier	E_1	E_2	G_{12}	ν_{12}	ν_{23}
E_{1f}	0.5	↓ 0.5		→ 0.8		
E_{1f}	2	↑ 2		→ 1.2		
E_{2f}	0.5		↓ 0.6			↑ 1.4
E_{2f}	2		↑ 2.2			→ 1.2
G_{12f}	0.5			→ 0.7		
G_{12f}	2			↑ 1.7		
ν_{12f}	0.5				→ 0.8	↑ 1.4
ν_{12f}	2				→ 1.2	↓ 0.1
ν_{23f}	0.5					→ 0.8
ν_{23f}	2					
E_m	0.5		↓ 0.5			↓ 0.1
E_m	2		↑ 1.9	→ 1.2		→ 1.3
ν_m	0.5				→ 0.8	
ν_m	2			→ 0.8		→ 1.3

Peer-reviewed version available at Materials 2019, 12, 1885; doi:10.3390/ma12121885

3.4 Macroscale modelling

Macroscale modelling was used to obtain relevant boundary conditions for the RVE, but also to confirm that the three point bending simulation using homogenised material properties behaves correctly. The simulation results are in good agreement with measured strain gauge and force cell values (Figure 8), although the measurements show a non-linear dependency, which is not captured by the model. In a similar way to what was done for the microscale modelling, a one-at-a-time sensitivity analysis was conducted by doubling and halving the homogenised material constants. E_1 could not be halved because the resulting displacements were too large for a stable solution to be found. Instead, a factor of 0.75 was chosen for the reduced E_1 case. Looking at the relative maximum von Mises stress, strain in fiber direction and center roller displacement it appears like E_1 is the main governing parameter in three point bending, while E_2 and G_{12} have only a weak effect on simulated component behaviour. E_1 is affected only by E_{1f} (Table 3) and therefore E_{1f} is the only constituent property that needs to be known accurately for macroscale modelling the bending of UD CFRP beams. Even an isotropic assumption leads only to a 3% error, meaning that the anisotropy is not essential to be included in the model. However, these results are only for three point bending and the transverse properties could play a larger role in other load cases.

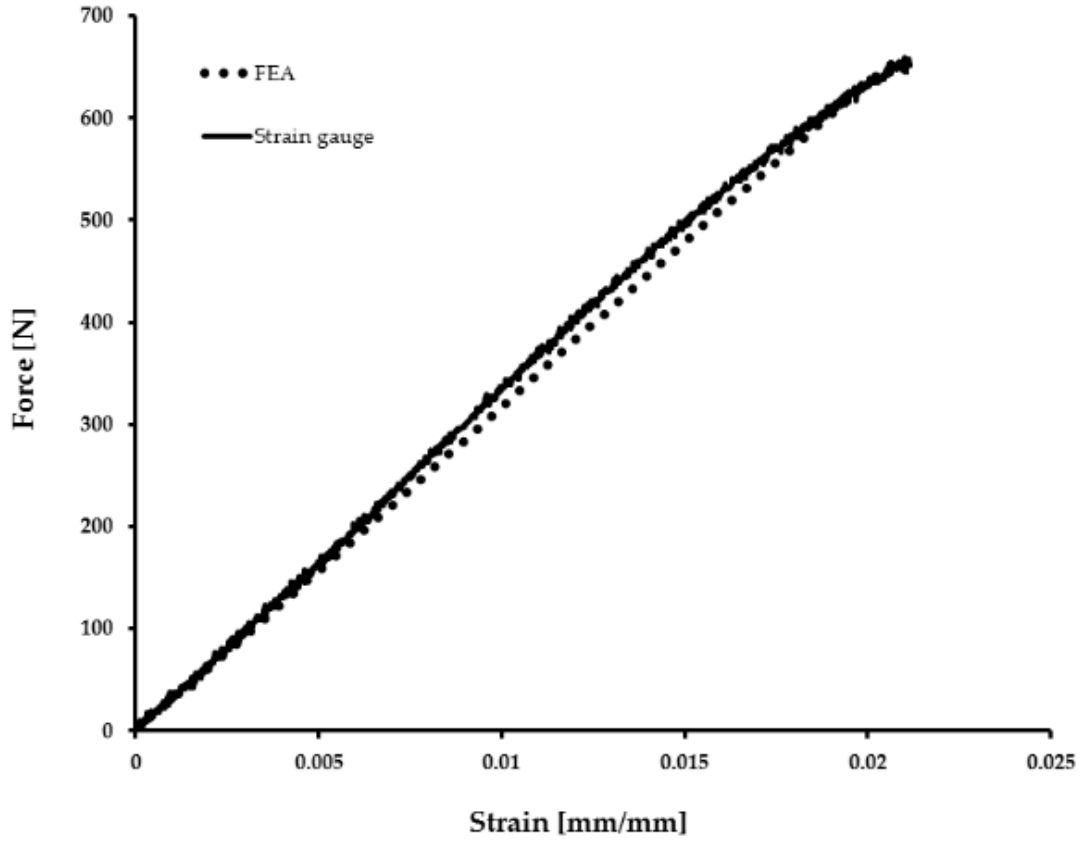

Figure 8. Comparison of simulated and experimental response in three point bending.

The homogenised material properties were verified using various macroscopic experiments. Results obtained using uniaxial tensile testing, uniaxial compression testing, transverse compression, flexural testing, quasi-static elasticity imaging (QSEI), analytical formulas and homogenisation of the micromechanical FE model are summarized in Table 4. G_{12} and ν_{23} are the only parameters where discrepancy is seen. The first was not directly measured and the latter was obtained from transverse compression where boundary conditions and specimen geometry, especially the length, could affect the results as well as the location of the virtual strain gauges on the cross-section.

Table 4. Summary of simulated and measured composite properties.

	E_1 [GPa]	E_2 [GPa]	G_{12} [GPa]	ν_{12}	ν_{23}
Uniaxial tension	148			0.29	
Uniaxial compression	135			0.29	
Transverse compression		7			0.5
Flexural testing	152				
QSEI [45]	155	7	10	0.29	
Analytical [20]	156	10	5.3	0.25	0.29
RVE FEA	158	9	6.8	0.25	0.34

3.5 Effect of defects

The last step of the multiscale modelling approach is to use the boundary conditions obtained from macroscale hot spot analysis for loading an RVE with a known defect. A resin-rich area in the microstructure is used to represent the microstructure with porosity (Figure 6). The lack of reinforcement fibers causes a local increase in strain and the surrounding fibers have to carry the load (Figure 9). However, this type of matrix defect does not adversely affect the measured flexural strength (Table 5). On the other hand, apparent ILSS tests indicate that porosity reduces the shear strength of the CFRP material and failure occurs in the center plane (1-3) of the specimen. Changing the RVE load case to correspond with the failure location observed in ILSS tests and looking at the shear strain components shows the effect of the resin-rich zone (Figure 10). As expected, heterogeneities in the microstructure cause local effects which can be quantified using the modelling approach presented here.

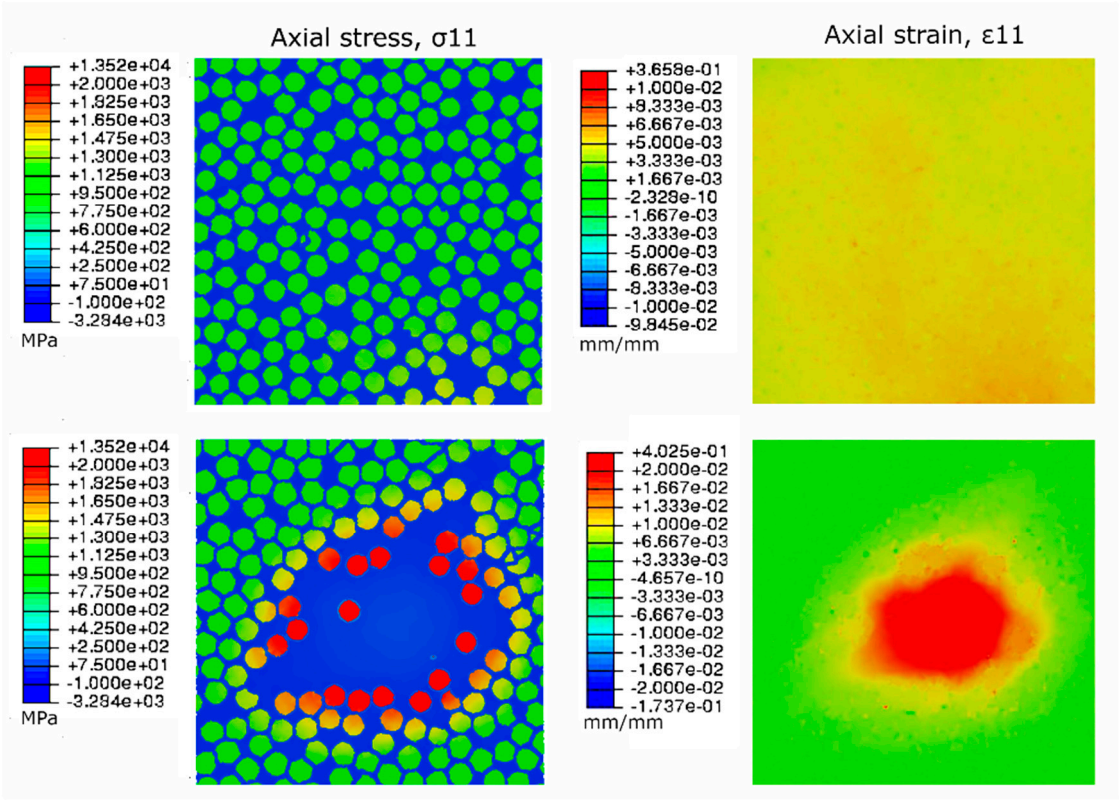

Figure 9. Comparison of reference microstructure (top) and resin-rich defect (bottom) in tension-dominated loading.

Peer-reviewed version available at Materials 2019, 12, 1885; doi:10.3390/ma12121885

Table 5. Comparison of strengths in defective and pristine samples.

Material	Flexural strength [MPa]	Apparent ILSS [MPa]
Reference	3120 ± 30	93.9 ± 0.2
Porous	3150 ± 132	73.1 ± 3.1

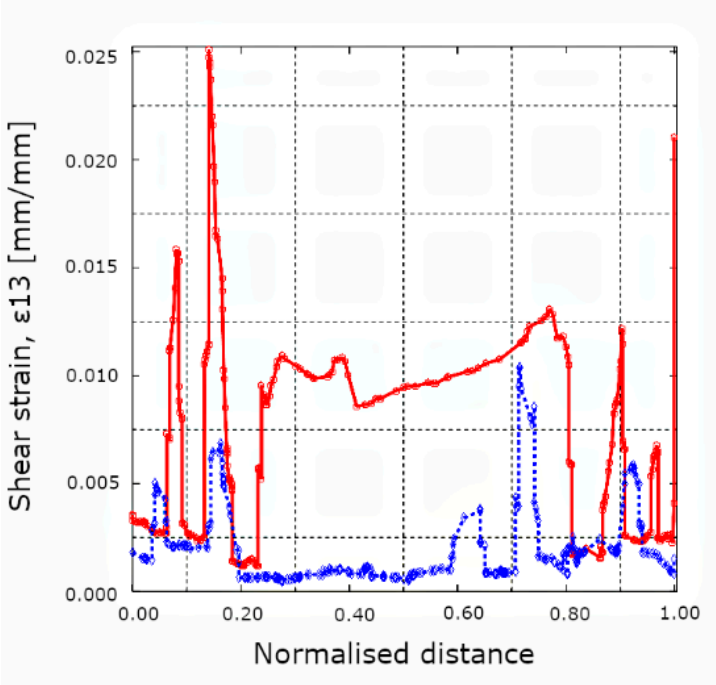

Figure 10. Line plots of the shear strains at the center (red) of the resin-rich microstructure and at the bottom (blue) in a shear-dominated load case.

4. Conclusions

A micromechanics-based model was created to estimate the effect of defects in unidirectional carbon fiber composites. The modelling approach requires the following inputs: fiber and resin properties, microstructure, macroscale load cases, boundary conditions and defect morphology and location.

- Fiber and resin properties given by manufacturers should be taken with caution, considering the measurement methodology is not known. Determining constituent properties with nanoindentation gives poor results for both longitudinal fiber and matrix properties. The phenomena could be attributed to nanoscale buckling of the fiber and a constraint effect in the matrix respectively. Transverse nanoindentation results of the fiber were closer to inverse micromechanics solutions and literature values of similar fibers. Despite the uncertainty in input parameters, the homogenised composite properties were in good agreement with experimental verifications.
- SEM images were successfully segmented algorithmically enabling the generation of a representative mesh of the microstructure. However, the use of 2D micrographs omits fiber waviness effects and defect morphology.
- Macroscale simulations were in good agreement with experimental work both in terms of elastic response and failure location. A sensitivity analysis showed that only the longitudinal modulus of the composite plays a significant role in the macroscale response. Furthermore, that parameter is mainly affected by the longitudinal fiber modulus, which is typically known. In fact, transverse properties are insignificant to a degree where an assumption of isotropic material properties leads only to a 3% error in stress/strain. However, three-point bending was the only load case used.
- A batch of high-porosity material was produced and the effect of porosity was simulated using a resin-rich area in the microstructure. The simulations show stress and strain concentrations in the fibers and matrix due to the heterogeneous microstructure. However, long-beam bending

experiments showed no difference in strength between reference and porous samples. This can be attributed to the load sharing mechanism of unidirectional reinforcement fibers in predominantly tensile loading. However, short-beam bending experiments showed a 20% reduction in apparent shear strength for the samples with porosity. The effect of matrix defects on shear strength was simulated by looking at the shear strains in the center plane where failure occurred. The results depict a highly strained matrix at the resin-rich zone compared to a homogeneous microstructure.

The approach presented here can be used to estimate the residual strength of a component with a known microscale defect. The component and load case used in this paper is simple and future work should include validating the approach for other component geometries and loads.

Author Contributions: conceptualization, K-N.A.; methodology, K-N.A, A.L, T.A.; software, A.L.; validation, K-N.A.; formal analysis, K-N.A., A.L.; investigation, K-N.A.; resources, K-N.A., P.V., A.L.; data curation, K-N.A, A.L.; writing—original draft preparation, K-N.A.; writing—review and editing, K-N.A., D.S., P.V.; visualization, K-N.A., A.L.; supervision, P.V.; project administration, P.V.; funding acquisition, P.V.

Funding: This research was funded by Business Finland FIMECC program and the APC was funded by Aalto University.

Conflicts of Interest: The authors declare no conflict of interest. The funders had no role in the design of the study; in the collection, analyses, or interpretation of data; in the writing of the manuscript, or in the decision to publish the results.

References

1. Rizzo, P.; di Scalea, L. Acoustic emission monitoring of carbon-fiber-reinforced-polymer bridge stay cables in large-scale testing. *Experimental Mechanics* **2001**, 41, pp. 282-290. DOI:10.1007/BF02323146
2. Rebel, G.; Verreet, R.; Ridge, I.M.L. Lightweight ropes for lifting applications. In: Proceedings of the OIPEEC Conference, Athens, Greece, 2006, pp. 33-54.
3. Antin, K-N.; Machado, M.A.; Santos, T.G.; Vilaça, P. Evaluation of different non-destructive testing methods to detect imperfections in unidirectional carbon fiber composite ropes. *Journal of Nondestructive Evaluation* **2019**, 38. DOI:10.1007/s10921-019-0564-y
4. Machado, M.A.; Antin, K-N.; Rosado, L.S.; Vilaça, P.; Santos, T.G. Contactless high-speed eddy current inspection of unidirectional carbon fiber reinforced polymer. *Composites Part B: Engineering* **2019**, 168, pp. 226-235. DOI:10.1016/j.compositesb.2018.12.021
5. Hedgepeth, J.M.; van Dyke, P. Local stress concentrations in imperfect filamentary composite materials. *Journal of Composite Materials* **1967**, 1, pp. 294-309.
6. Landis, C.M.; McMeeking, R.M. Stress concentrations in composites with interface sliding, matrix stiffness and uneven fiber spacing using shear lag theory. *International Journal of Solids and Structures* **1999**, 36, pp. 4333-4361.
7. Otero, J.A.; Rodriguez-Ramos, R.; Bravo-Castillero, J.; Guinovart-Diaz, R.; Sabina, F.J.; Monsivais, G. Semi-analytical method for computing effective properties in elastic composite under imperfect contact. *International Journal of Solids and Structures* **2013**, 50, pp. 609-622. DOI:10.1016/j.ijsolstr.2012.11.001
8. Sun, C.T.; Vaidya, R.S. Prediction of composite properties from a representative volume element. *Composites Science and Technology* **1996**, 56, pp. 171-179.
9. Mishnaevsky Jr., L.; Broensted, P. Micromechanical modeling of damage and fracture of unidirectional fiber reinforced composites: A review. *Computational Materials Science* **2009**, 44, pp. 1351-1359. DOI:10.1016/j.commatsci.2008.09.004
10. Wongsto, A.; Li, S. Micromechanical FE analysis of UD fibre-reinforced composites with fibres distributed at random over the transverse cross-section. *Composites Part A* **2005**, 36, pp. 1246-1266. DOI:10.1016/j.compositesa.2005.01.010
11. Dong, C. Effects of Process-Induced Voids on the Properties of Fibre Reinforced Composites. *Journal of Materials Science & Technology* **2016**, 7, pp. 597-604. DOI: 10.1016/j.jmst.2016.04.011
12. Swolfs, Y.; Gorbatikh, L.; Romanov, V.S.; Orlova, S.; Lomov, S.V.; Verpoest, I. Stress concentrations in an impregnated fibre bundle with random fibre packing. *Composites Science and Technology* **2013**, 74, pp. 113-120. DOI:10.1016/j.compscitech.2012.10.013

13. Vaughan, T.J.; McCarthy, C.T. Micromechanical modelling of the transverse damage behaviour in fibre reinforced composites. *Composites Science and Technology* **2011,** 71, pp. 388-396. DOI:10.1016/j.compscitech.2010.12.006
14. Maurin, R.; Davies, P.; Baral, N.; Baley, C. Transverse properties of carbon fibres by nano-indentation and micro-mechanics. *Applied Composite Materials* **2008**, 15, pp. 61-73. DOI:10.1007/s10443-008-9057-3
15. Beicha, D.; Kanit, T.; Brunet, Y.; Imad, A.; El Moumen, A.; Khelfaoui, Y. Effective transverse elastic properties of unidirectional fiber reinforced composites. *Mechanics of Materials* **2016**, 102, pp. 47-53. DOI:10.1016/j.mechmat.2016.08.010
16. Schumacher, D.; Antin, K-N.; Zscherpel, U.; Vilaça, P. Application of different X-ray techniques to improve in-service carbon fiber reinforced rope inspection. *Journal of Nondestructive Evaluation* **2017**, 36, pp. 1-14. DOI:10.1007/s10921-017-0441-5
17. Halpin, J.C.; Kardos, J.L. The Halpin-Tsai equations: A review. *Polymer Engineering and Science* ***1976***, 16, pp. 344-352.
18. Sarlin, E.; von Essen, M.; Palola, S.; Lindgren, M.; Kallio, P.; Vuorinen, J. Determination of environmental degradation of matrix and fiber materials with a novel, stastically reliable micro-robotic approach. In: Proceedings of the 17th European Conference on Composite Materials ECCM17, München, Germany, 2016.
19. Ilankeeran, P.K.; Mohite, P.M.; Kamle, S. Axial tensile testing of single fibres. *Modern Mechanical Engineering* **2012**, 2, pp. 151-156. DOI:10.4236/mme.2012.24020
20. Chamis, C.C. Simplified composite micromechanics equations for hygral, thermal and mechanical properties. NASA Technical Memorandum 83320, In: 38th Annual Conference of the Society of the Plastics Industry, Houston, Texas, USA, 1983.
21. Mounier, D.; Poilane, C.; Bucher, C.; Picart, P. Evaluation of transverse elastic properties of fibers used in composite materials by laser resonant ultrasound spectroscopy. In: Proceedings of the Acoustics Conference, Nantes, France, 2012.
22. Soden, P.D.; Hinton, M.J.; Kaddour, A.S. Lamina properties, lay-up configurations and loading conditions for a range of fibre-reinforced composite laminates. *Composites Science and Technology* **1998**, 58, pp. 1011-1022.
23. Turon, A.; Costa, J.; Maimi, P.; Trias, D.; Mayugo, J.A. A progressive damage model for unidirectional fibre-reinforced composites based on fibre fragmentation. Part I: Formulation. *Composites Science and Technology* **2005**, 65, pp. 2039-2048. DOI:10.1016/j.compscitech.2005.04.012
24. Blassiau, S.; Thionnet, A.; Bunsell, A.R. Micromechanisms of load transfer in a unidirectional carbon fibre–reinforced epoxy composite due to fibre failures. Part 1: Micromechanisms and 3D analysis of load transfer: The elastic case. *Composite Structures* **2006**, 74, pp. 303-318. DOI:10.1016/j.compstruct.2005.04.013
25. Behzadi, S.; Jones, F.R. The effect of temperature on stress transfer between a broken fibre and the adjacent fibres in unidirectional fibre composites. *Composites Science and Technology* **2010**, 68, pp. 2690-2696. DOI:10.1016/j.compscitech.2008.04.046
26. Bouaoune, L.; Brunet, Y.; El Moumen, A.; Kanit, T.; Mazouz, H. Random versus periodic microstructures for elasticity of fibers reinforced composites. *Composites Part B* **2016**, 103, pp. 68-73. DOI:10.1016/j.compositesb.2016.08.026
27. Melro, A.R.; Camanho, P.P.; Pinho, S.T. Generation of random distribution of fibres in long-fibre reinforced composites. *Composites Science and Technology* **2008**, 68, pp. 2092-2102. DOI:10.1016/j.compscitech.2008.03.013
28. Swolfs, Y.; Verpoest, I.; Gorbatikh, L. Issues in strength models for unidirectional fibre-reinforced composites related to Weibull distributions, fibre packings and boundary effects. *Composites Science and Technology* **2015**, 114, pp. 42-49. DOI:10.1016/j.compscitech.2015.04.002
29. Okabe, T.; Takeda, N.; Kamoshida, Y.; Shimizu, M.; Curtin, W.A. A 3D shear-lag model considering micro-damage and statistical strength prediction of unidirectional fiber-reinforced composites. *Composites Science and Technology* **2001**, 61, pp. 1773-1787.
30. Trias, D.; Costa, J.; Mayugo, J.A.; Hurtado, J.E. Random models versus periodic models for fibre reinforced composites. *Computational Materials Science* **2006**, 38, pp. 316-324. DOI:10.1016/j.commatsci.2006.03.005
31. Holmberg, K.; Laukkanen, A.; Turunen, E.; Laitinen, T. Wear resistance optimisation of composite coatings by computational microstructural modelling. *Surface and Coatings Technology* **2014**, 247, pp. 1-13. DOI:10.1016/j.surfcoat.2014.02.019

32. Orell, O.; Vuorinen, J.; Jokinen, J.; Kettunen, H.; Hytönen, P.; Turunen, J.; Kanerva, M. Characterization of elastic constants of anisotropic composites in compression using digital image correlation. *Composite Structures* **2018**, 185, pp. 176-185. DOI:10.1016/j.compstruct.2017.11.008
33. Haj-Ali, R.; Kilic, H. Nonlinear constitutive model for pultruded FRP composites. *Mechanics of Materials* **2003**, 35, pp. 791-801. DOI:10.1016/S0167-6636(02)00207-7
34. Fiedler, B.; Holst, S.; Hobbiebrunken, T.; Hojo, M.; Schulte, K. Modelling of the initial failure of CFRP structures by partial discretisation: A micro/macro-mechanical approach of first ply failure. *Advanced Composite Letters* **2004**, 13. DOI:10.1177/096369350401300501
35. Fliegener, S.; Luke, M.; Gumbsch, P. 3D microstructure modeling of long fiber reinforced thermoplastics. *Composites Science and Technology* **2014**, 104, pp. 136-145. DOI:10.1016/j.compscitech.2014.09.009
36. Miyagawa, H.; Mase, T.; Sato, C.; Drown, E.; Drzal, L.T.; Ikegami, K. Comparison of experimental and theoretical transverse elastic modulus of carbon fibers. *Carbon* **2006**, 44, pp. 2002-2008. DOI:10.1016/j.carbon.2006.01.026
37. Diss, P.; Lamon, J.; Carpentier, L.; Loubet, J.L.; Kapsa, P. Sharp indentation behavior of carbon/carbon composites and varities of carbon. *Carbon* **2002**, 40, pp. 2567-2579.
38. Oliver, W.C.; Pharr, G.M. An improved technique for determining hardness and elastic modulus using load and displacement sensing indentation experiments. *Journal of Materials Research* **1992**, 7, pp. 1564-1583. DOI:10.1557/JMR.1992.1564
39. Oliver, W.C.; Pharr, G.M. Measurement of hardness and elastic modulus by instrumented indentation: Advances in understanding and refinements to methodology. *Journal of Materials Research* **2004**, 19, pp. 3-20. DOI:10.1557/jmr.2004.19.1.3
40. Vlassak, J.J.; Ciavarella, M.; Barber, J.R.; Wang, X. The indentation modulus of elastically anisotropic materials for indenters of arbitrary shape. Journal of the *Mechanics and Physics of Solids* **2003**, 5, pp. 1701-1721. DOI:10.1016/S0022-5096(03)00066-8
41. Delafargue, A.; Ulm, F-J. Explicit approximations of the indentation modulus of elastically orthotropic solids for conical indenters. *International Journal of Solids and Structures* **2004**, 41, pp. 7351–7360. DOI:10.1016/j.ijsolstr.2004.06.019
42. Csanadi, T.; Nemeth, D.; Zhang, C.; Dusza J. Nanoindentation derived elastic constants of carbon fibres and their nanostructural based predictions. *Carbon* **2017**, 119, pp. 314-325. DOI:10.1016/j.carbon.2017.04.048
43. Hashin, Z. Thin interphase/imperfect interface in elasticity with application to coated fiber composites. *Journal of the Mechanics and Physics of Solids* ***2002***, 50, pp. 2509-2537.
44. Tang, Z.; Wang, C.; Yu, Y. Failure response of fiber-epoxy unidirectional laminate under transverse tensile/compressive loading using finite-volume micromechanics. *Composites Part B* **2015**, 79, pp. 331-341. DOI: 10.1016/j.compositesb.2015.04.054
45. Smyl, D.; Antin, K-N.; Dong, L.; Bossuyt, S. Coupled digital image correlation and quasi-static elasticity imaging of inhomogeneous orthotropic composite structures. *Inverse Problems* **2018**, 34. DOI:10.1088/1361-6420/aae793
46. Qiao, Y.; Bisagni, C.; Bai, Y. Experimental investigation and numerical simulation of unidirectional carbon fiber composite under multi-axial loadings. *Composites Part B* **2017**, 124, pp. 190-206. DOI:10.1016/j.compositesb.2017.05.034
47. Oscan, S.; Tezcan, J.; Filip, P. Microstructure and elastic properties of individual components of C/C composites. *Carbon* **2009**, 47, pp. 3403-3414. DOI:10.1016/j.carbon.2009.07.057
48. Marx, D.T.; Riester, L. Mechanical properties of carbon-carbon composite components determined using nanoindentation. *Carbon* **1999**, 37, pp. 1679-1684.
49. Leatherbarrow, A.; Wu, H. Mechanical behaviour of the constituents inside carbon-fibre/carbon-silicon carbide composites characterised by nano-indentation. *Journal of the European Ceramic Society* **2012**, 32, pp. 579-588. DOI:10.1016/j.jeurceramsoc.2011.09.026
50. Hardiman, M.; Vaughan, T.J.; McCarthy, C.T. The effect of fibre constraint in the nanoindentation of fibrous composite microstructures: A finite element investigation. *Computational Materials Science* **2012**, 64, pp. 162-167. DOI:10.1016/j.commatsci.2012.04.033